

Discovery of a New Spectral Transition in Swift J0243.6+6124 in the Sub-Eddington Regime

Bo-Yan Chen ,^{1,2} Shu Zhang ,¹ Qing-Cang Shui ,^{1,2} Peng-Ju Wang ,³ Long Ji ,⁴ Ling-Da Kong ,³ Shuang-Nan Zhang ,^{1,2} Hua Feng ,¹ Yu-Peng Chen ,¹ Ming-Yu Ge ,^{1,2} Jing-Qiang Peng ,^{1,2} AND Wen-zhong Li ,^{1,2}

¹State Key Laboratory of Particle Astrophysics, Institute of High Energy Physics, Chinese Academy of Sciences, Beijing 100049, People's Republic of China

²University of Chinese Academy of Sciences, Chinese Academy of Sciences, 100049 Beijing, People's Republic of China

³Institute für Astronomie und Astrophysik, Kepler Center for Astro and Particle Physics, Eberhard Karls Universität, Sand 1, D-72076 Tübingen, Germany

⁴School of Physics and Astronomy, Sun Yat-Sen University, Zhuhai, 519082, People's Republic of China

ABSTRACT

We have conducted a detailed spectral analysis of Swift J0243.6+6124 in its sub-Eddington regime observed by Insight-HXMT and NICER during a series of outbursts including the giant one in 2018, and discovered a new transition at $L_t \sim 4.5 \times 10^{37}$ erg s⁻¹ accompanied by the evolution of the spectral parameters, in particular a significant turnover of the blackbody normalization. L_t in the sub-Eddington regime represents the fifth transition luminosity identified so far, further increasing the complexity of Swift J0243.6+6124 and may be accounted via introducing a multipolar magnetic field configuration, where weak ($\sim 2.8 \times 10^{12}$ G) and strong ($\sim 1.6 \times 10^{13}$ G) magnetic poles govern the emission at different accretion rates. Such a magnetic field configuration is equivalent to a relatively weak pure dipole magnetic field of $\sim 6.6 \times 10^{12}$ G on the scale of the magnetosphere radius, and allows the local magnetic field of the neutron star to exceed 10^{13} G.

Keywords: Accretion ; Magnetic fields ; Neutron stars;

1. INTRODUCTION

Accreting X-ray pulsars (AXRPs) in high-mass X-ray binaries are highly magnetized neutron stars that accrete matter from their early-type companions through either stellar wind capture or Roche-lobe overflow (Mushtukov & Tsygankov 2022). The strong magnetic field, typically $B \sim 10^{12}$ – 10^{13} G, truncates the accretion flow at the magnetospheric radius R_m , where the infalling plasma is forced to follow the magnetic field lines and is directed toward the magnetic poles. There, the material releases its gravitational potential energy as

bychen@ihep.ac.cn

Corresponding author: Shu Zhang
 szhang@ihep.ac.cn

Corresponding author: Qing-Cang Shui
 shuiqc@ihep.ac.cn

intense X-ray radiation (Staubert et al. 2019). Extensive theoretical studies have established that the geometry and physical conditions above the polar caps evolve markedly with the mass accretion rate, \dot{M} , giving rise to complex variations in both timing and spectral properties during outbursts(Basko & Sunyaev 1975; Burnard et al. 1991; Becker et al. 2012; Mushtukov et al. 2015a; Becker & Wolff 2022). Such evolutions are generally associated with characteristic luminosities.

Transitional luminosities are ubiquitous in AXRPs, with diverse physical origins proposed in the literature(Reig & Nespoli 2013; Xiao & Ji 2024). At $L_X \sim 10^{37}$ – 38 erg s⁻¹, the so-called critical luminosity, L_{crit} , is often invoked to explain abrupt changes in the spectral continuum(Becker et al. 2012). Theoretically, once L_X exceeds L_{crit} , the centroid energy of the cyclotron resonance scattering feature (CRSF), E_{cyc} , is predicted to switch from a positive to a negative correlation. This bimodality coincides with transitions in

hardness–intensity diagrams (HIDs) and breaks in the evolution of spectral parameters(Reig & Nespoli 2013; Staubert et al. 2019).

In the subcritical regime ($L_X < 10^{37} \text{ erg s}^{-1}$), spectral evolution may be driven by multiple mechanisms. Far below L_{crit} (e.g., $L_X \sim 10^{34-35} \text{ erg s}^{-1}$), radiation-dominated shock may collapse into collisionless shock and vacuum polarization effects may dominate, as discussed for the extremely low transition luminosity in 1A 0535+262 (Langer & Rappaport 1982; Xiao & Ji 2024). As the mass-accretion rate increases to yield $L_X \sim 10^{36-37} \text{ erg s}^{-1}$, Coulomb interaction become the primary deceleration mechanism after the gas shock, defining a Coulomb luminosity, L_{Coul} (Becker et al. 2012; Langer & Rappaport 1982). In this regime, matter decelerates above the polar cap via Coulomb interaction and emits thermal radiation from the surface hotspot; the hybrid emission pattern resulting from the coexistence of pencil and fan beams persists until L_{crit} . (Burnard et al. 1991). Overall, above $L_X \sim 10^{36} \text{ erg s}^{-1}$, only L_{Coul} and L_{crit} serve as viable transition luminosities, while observationally most AXRPs exhibit only a single spectral transition(Reig & Nespoli 2013).

The Swift J0243.6+6124 was discovered by the Swift/BAT telescope at a flux of 80 mCrab in October 2017 (Kennea et al. 2017; Cenko et al. 2017). Subsequently, the giant outburst that occurred in 2017 reached a peak luminosity of $L_X \sim 2 \times 10^{39} \text{ erg s}^{-1}$, calculated under the assumption of a distance of 6.8 kpc to the companion star, as reported by Bailer-Jones et al. (2018) based on Gaia DR2 parallax measurements. Even when adopting the latest Gaia DR3 distance of $5.2 \pm 0.3 \text{ kpc}$ (source ID: 465628193526364416; Bailer-Jones et al. 2021), the peak luminosity remains at $L_X \sim 1 \times 10^{39} \text{ erg s}^{-1}$, still exceeding the Eddington limit for a typical neutron star, confirming Swift J0243.6+6124 as the first Galactic ultraluminous X-ray pulsar (Tsygankov et al. 2018). Timing analysis revealed a spin period of $P_{\text{spin}} \sim 9.8 \text{ s}$ and an optical counterpart classified as an O9.5 Ve star, confirming its BeXRB nature(Kennea et al. 2017; Bahramian et al. 2017; Cenko et al. 2017; Doroshenko et al. 2018; Kouroubatzakis et al. 2017; Yamanaka et al. 2017; Reig et al. 2020).

Since discovery, Swift J0243.6+6124 has undergone a series of subsequent outbursts. Even at the faintest luminosity of $L_X \sim 3 \times 10^{34} \text{ erg s}^{-1}$ (0.1 – 200 keV, 6.8 kpc), NuSTAR detected no propeller effect, demonstrating that its accretion luminosity covers six orders of magnitude ($10^{34-39} \text{ erg s}^{-1}$), and making it an exemplary source for studying the full accretion evolution in XRPs(Doroshenko et al. 2020).

In the sub-Eddington regime, the broadband X-ray spectrum of Swift J0243.6+6124 can be well described by an absorbed cutoffpl and a blackbody component. As the luminosity increases, the Fe K α emission becomes prominent, exhibiting a narrow-to-broad line transition(Jaisawal et al. 2019; Kong et al. 2020; Bahramian et al. 2017; Jaisawal et al. 2018); two additional low-temperature blackbody components gradually emerge, which may correspond to radiation from an optically thick outflow and from the top of the accretion column(Tao et al. 2019). The optically thick outflow is likely produced by the transition from a gas-pressure-dominated (GPD) to a radiation-pressure-dominated (RPD) disc. (Tao et al. 2019; van den Eijnden et al. 2019; Doroshenko et al. 2020; Wang et al. 2020).

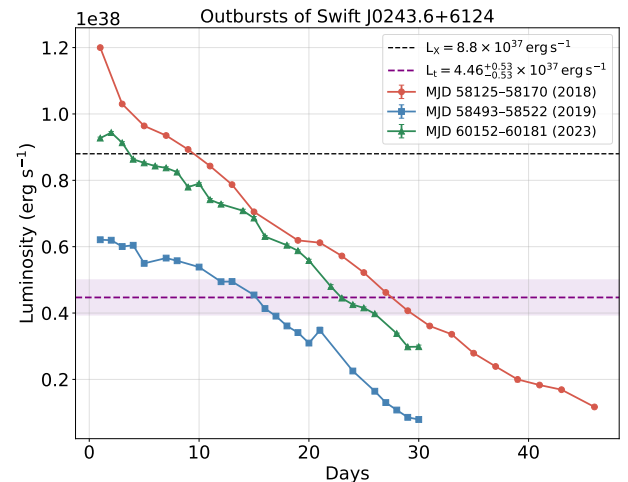


Figure 1. Bolometric luminosity evolution during the decay phases of three outbursts. The luminosity is derived from Insight-HXMT observations in the 2–150 keV band. The red, blue, and green curves correspond to the outbursts in 2018 (MJD 58125–58170), 2019 (MJD 58493–58523), and 2023 (MJD 60152–60181), respectively. The purple dashed line marks the newly identified transition luminosity (with the uncertainty interval at the 90% confidence level marked by the purple bar), while the black dashed line represents the previously reported critical luminosity L_1 of the source(Kong et al. 2020). The x-axis shows the elapsed days since the first data point used for each outburst.

Several transition luminosities have been discovered in Swift J0243.6+6124. From the pulse fraction evolution one infers a transition luminosity of $\sim 7.7 \times 10^{38} \text{ erg s}^{-1}$ (2 – 150 keV, 6.8 kpc, using Insight-HXMT)(Wang et al. 2020). Insight-HXMT observations of both spectral parameters and pulse-profile evolution confirm two spectral transition luminosities at $L_1 \sim 1.5 \times 10^{38} \text{ erg s}^{-1}$ and $L_2 \sim 4.4 \times 10^{38} \text{ erg s}^{-1}$ (2 – 150 keV, 6.8 kpc); the latter is interpreted as the critical luminosity, yielding

a magnetic field estimate of $B \sim 2.4 \times 10^{13}$ G, which is consistent with the discovery of 146 keV CRSF line and at odds with weaker dipolar field estimates of a few $\times 10^{12}$ G, indicating a multipolar magnetic configuration(Kong et al. 2020; Doroshenko et al. 2020; Kong et al. 2022; Tsygankov et al. 2018). Long-term NICER monitoring also provides the full spectral parameter evolution and reveals transitions, but NICER’s narrowband yields results that differ markedly from broadband studies (Kong et al. 2020; Chhotaray et al. 2024).At lower luminosities, the NICER pulse-profile evolution confirms a transition at $L_t \sim 7 \times 10^{36}$ erg s $^{-1}$ (2–150 keV; 5.2 kpc), likely marking the onset of significant Coulomb deceleration(Serim et al. 2023).

Between MJD 58125 and MJD 60181, one giant outburst and two normal outbursts of Swift J0243.6+6124 were recorded by Insight-HXMT. In this paper, we present a detailed spectral analysis of Swift J0243.6+6124—the first Galactic ultraluminous X-ray pulsar—in its sub-Eddington accretion regime, using sub-Eddington observations from Insight-HXMT complemented by contemporaneous NICER data. Considering that the updated distance affects the derived parameters throughout our analysis, we adopt the latest Gaia DR3 distance of 5.2 ± 0.3 kpc (Bailer-Jones et al. 2021) uniformly in this work. The rest of the paper is organized as follows: Section 2 describes the observations and data-reduction strategy; Section 3 presents the luminosity and spectral-evolution results; Section 4 discusses these findings; and Section 5 summarizes our conclusions.

2. OBSERVATIONS AND DATA REDUCTION

2.1. *Insight-HXMT*

The Hard X-ray Modulation Telescope (Insight-HXMT) was launched on June 15, 2017. It features a wide energy band (1–250 keV), a large effective area at high energies, and is free from the pile-up effect for bright sources(Zhang et al. 2014, 2020). Insight-HXMT consists of three collimated telescopes: the High Energy X-ray telescope (HE), the Medium Energy X-ray telescope (ME), and the Low Energy X-ray telescope (LE). Their respective collecting areas and energy ranges are approximately 5100 cm^2 over 20–250 keV for HE, 952 cm^2 over 5–30 keV for ME, and 384 cm^2 over 1–10 keV for LE. The primary fields of view (FoV) of LE, ME, and HE are $1.6^\circ \times 6^\circ$, $1^\circ \times 4^\circ$, and $1.1^\circ \times 5.7^\circ$, respectively (Liu et al. 2020; Cao et al. 2020; Chen et al. 2020).

From October 7, 2017 (MJD 58033) to February 21, 2018 (MJD 58170), Insight-HXMT triggered a total of 122 pointed exposures, sampling the entire giant out-

burst of Swift J0243.6+6124. In subsequent outbursts, Insight-HXMT observed the decay phases of two outbursts in 2019 and 2023, covering January 10, 2019 (MJD 58493) to February 9, 2019 (MJD 58523) and July 27, 2023 (MJD 60152) to August 25, 2023 (MJD 60181), respectively. Since the 2019 and 2023 outbursts did not exceed the Eddington luminosity (for a typical neutron star, $L_{\text{Edd}} \sim 1.8 \times 10^{38}$ erg s $^{-1}$ in the 2–150 keV band) and our focus is on the sub-Eddington regime, we selected observations from three decay intervals: January 7, 2018 (MJD 58125) to February 21, 2018 (MJD 58170), January 10, 2019 (MJD 58493) to February 9, 2019 (MJD 58523), and July 27, 2023 (MJD 60152) to August 25, 2023 (MJD 60181). The bolometric luminosity spans from 7.9×10^{36} erg s $^{-1}$ to 1.2×10^{38} erg s $^{-1}$ (2–150 keV, 5.2 kpc, see Figure 1). The data in the luminosity range of $1.2 \times 10^{38} – 1.8 \times 10^{38}$ erg s $^{-1}$ have already been investigated in detail by Kong et al. (2020), and are not discussed there.

In this work, we processed the data using the Insight-HXMT Data Analysis Software (HXMTDAS) v2.06 and applied barycenter correction and binary orbital correction using the `hbary` and `binCor` tools, respectively. The data were filtered using the Good Time Intervals (GTIs) recommended by the Insight-HXMT team, and only data with at least 300 s before and after the South Atlantic Anomaly (SAA) passages were used. In addition, since our study focuses on the low-luminosity regime, to improve the fitting quality we combined the observational data on a daily basis and re-binned the spectra using `grppha`. Depending on the instrument performance and specific requirements, we selectively employed certain energy bands; details are provided in subsequent sections.

2.2. *NICER*

The Neutron star Interior Composition Explorer (NICER) was launched in June 2017 and installed on the International Space Station. It is equipped with the X-ray Timing Instrument (XTI), designed to operate in the 0.2–12 keV energy range(Gendreau et al. 2016; Prigozhin et al. 2016). NICER observed the giant and subsequent normal X-ray outbursts between MJD 58029 (October 3, 2017) and MJD 58533 (February 19, 2019) with a net exposure time of 408 ks. In addition, NICER observed the recent 2023 outburst, accumulating approximately 104 ks of net exposure from observations conducted between June and September 2023 under observation IDs 6050390227–6050390277. We selected NICER data overlapping with the Insight-HXMT observation periods for spectral fitting. The unfiltered event data from NICER were processed using the `nicer12`

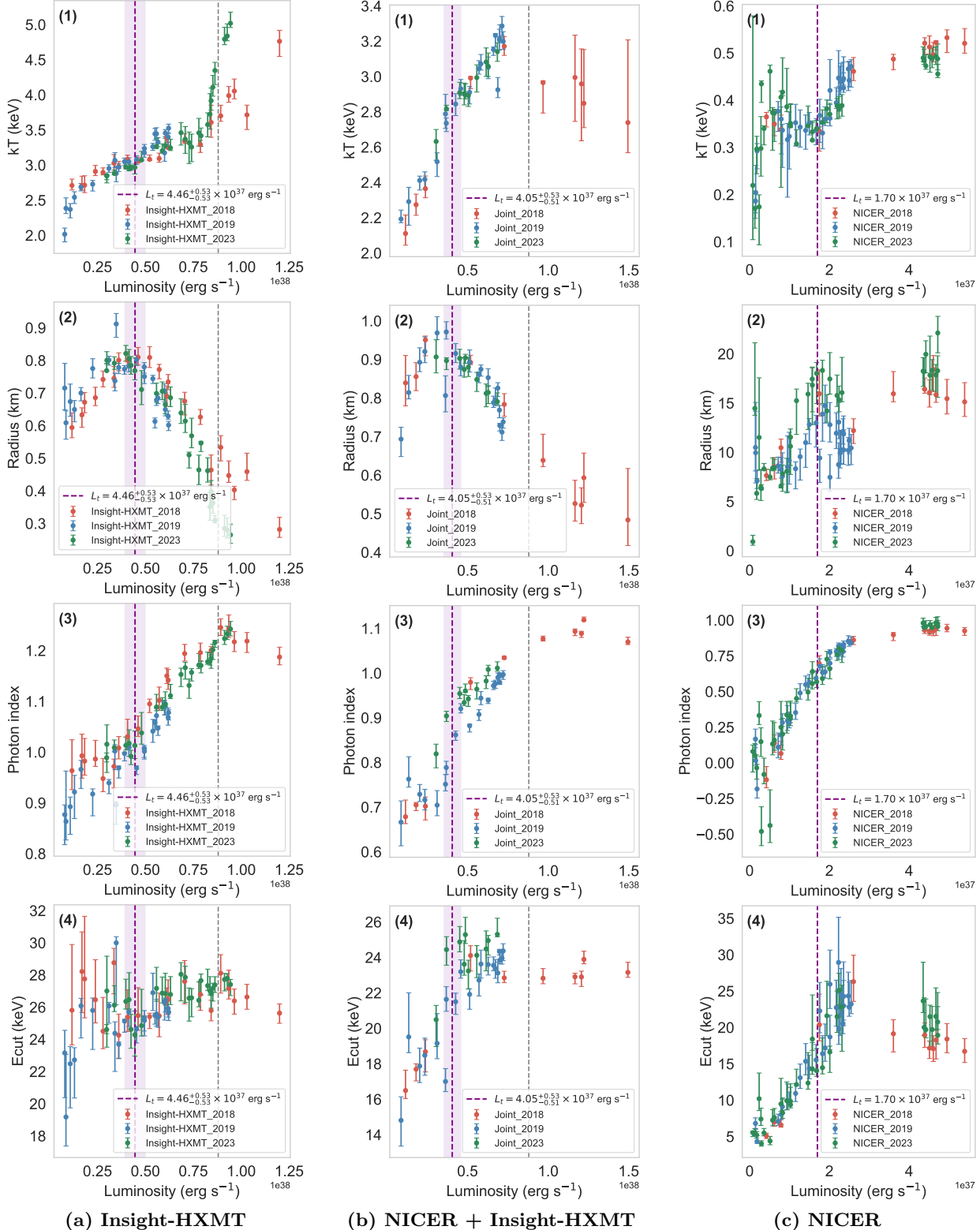


Figure 2. Parameter evolution versus luminosity derived from spectral fits performed with three instrument combinations. **Left:** Insight-HXMT only (LE: 2–10 keV; ME: 8–30 keV; HE: 28–100 keV), covering 2–100 keV in fitting, with luminosities evaluated over 2 – 150 keV; **Middle:** Joint fits in which NICER (0.7–10 keV) replaces the LE data when observations are within 24 hr (ME: 8–30 keV; HE: 28–100 keV); luminosities are also evaluated over 2 – 150 keV; **Right:** NICER-only narrowband fits (0.7–10 keV), with luminosities computed in the same energy band. The grey dashed line marks the adopted transition luminosity L_t (0.7–10 keV). The purple shaded band in the left and middle panels spans the 90% credible range for each data set.

pipeline within HEASOFT v6.30. The analysis was carried out with the gain version `xti20221001` under the condition that the calibration database files were available. Spectra were extracted using `nicerl3-spect` pipelines.

3. RESULTS

3.1. Luminosity Evolution

The spectrum of Swift J0243.6+6124 was modeled using `constant*tbabs*(bbodyrad+cutoffp1)` in XSPEC (version 12.13.1; Arnaud 1996), where the multiplicative `constant` accounts for cross-calibration uncertainties among different instruments. Within the luminosity range explored in this work, the iron $K\alpha$ line near 6.4 keV cannot be well constrained and has a negligible impact on the best-fit results; therefore, no additional Gaussian component was included. Parameter uncertainties were estimated using Markov Chain Monte Carlo (MCMC) sampling with 20,000 iterations, 40 walkers, and a burn-in phase of 2,000 steps, and are quoted at the 90% confidence level. We apply `constant*tbabs*cflux*(bbodyrad+cutoffp1)` to estimate the 2–150 keV luminosity, assuming a distance of 5.2 kpc reported in Bailer-Jones et al. (2021) based on Gaia DR3 parallax measurements of the companion star.

As can be seen, the luminosity ranges of the three results shown in Figure 2 are not identical. Here we provide a detailed description of the luminosity calculation adopted in this work. In Figure 2(a), where only Insight–HXMT data in the 2–100 keV band are fitted, we use `cflux` to compute the source flux in the 2–150 keV band and convert it into luminosity. In Figure 2(b), where a joint fit is performed over the 0.7–100 keV band, we calculate the source luminosity in the 2–150 keV band. In Figure 2(c), where only NICER data in the 0.7–10 keV band are fitted, we compute the 0.7–10 keV luminosity, in order to reproduce the results reported by Chhotaray et al. (2024).

To maintain consistency with previous studies (Kong et al. 2020; Wang et al. 2020; Kong et al. 2022), we primarily adopt the luminosity range obtained in Figure 2(a) for our discussion. The luminosity range derived in Figure 2(a) is $(7.9\text{--}120) \times 10^{36} \text{ erg s}^{-1}$, which covers the decay phases of all three outbursts, and this range is shown in Figure 1. We found that, in the 2–150 keV energy band, the luminosities derived from the joint fit are systematically higher by about 10% compared to the Insight–HXMT–only results. This offset is likely caused by the inclusion of the 0.7–2 keV band in the joint fit and does not affect the main results of this work.

3.2. Spectral Discrepancy with Different Telescope Configurations

Chhotaray et al. (2024) performed spectral fitting of long-term NICER data in the 0.7–10 keV band for Swift J0243.6+6124, deriving spectral-parameter evolutions over a luminosity range similar to that observed by Insight–HXMT (Kong et al. 2020), yet with markedly different values and trends. To address this discrepancy, we compare the spectral evolutions with data of NICER only, Insight–HXMT only and the joint Insight–HXMT/NICER observations, with results shown in Figure 2.

For Insight–HXMT we restrict the analysis to the 2–100 keV band (LE: 2–10 keV; ME: 8–30 keV; HE: 28–100 keV), omitting > 100 keV data dominated by background and 1–2 keV data showing instrumental artifacts. For NICER we adopt the 0.7–10 keV band to avoid calibration uncertainties below 0.4 keV, above 10.0 keV, and the edge-like feature near 0.5 keV (Chhotaray et al. 2024). Absorption is modeled with the Wilms abundance table and Verner photoionization cross sections and fits are evaluated using χ^2 statistics (Wilms et al. 2000). Based on Insight–HXMT calibration and previous NICER work, spectra are rebinned as follows: (1) NICER: a minimum of 30 counts per energy bin; (2) LE: channels 0–579 grouped in 5, channels 580–1535 in 10; (3) ME: channels 0–1023 grouped in 2; (4) HE: channels 0–255 grouped in 2. A `constant` component accounts for inter-instrument calibration, and the final model is `constant*tbabs*(bbodyrad+cutoffp1)`.

The parameter settings for each detector combination are as follows:

1. Insight–HXMT only: we use the 2–100 keV band with a systematic error of 1%. We initially allowed n_{H} to vary and found a mean value of $\sim 1.0 \times 10^{22} \text{ cm}^{-2}$, consistent with Chhotaray et al. (2024). For consistency, we fixed $n_{\text{H}} = 1.064 \times 10^{22} \text{ cm}^{-2}$ in all fits. The LE normalization constant was fixed at unity, while the ME and HE constants were left free to vary.

2. NICER only: we use the 0.7–10 keV band with a systematic error of 1.5% and fix $n_{\text{H}} = 1.064 \times 10^{22} \text{ cm}^{-2}$ to reproduce previous analyses in Chhotaray et al. (2024).

3. Joint NICER+Insight–HXMT: we extend the bandpass to 0.7–100 keV, fix the NICER constant at unity and set $n_{\text{H}} = 1.064 \times 10^{22} \text{ cm}^{-2}$.

The spectral-evolution results for the three telescope configurations are shown in Figure 2. In Group (a) (Insight–HXMT only) the reduced- χ^2 remains ~ 1 throughout the full luminosity range, indicating that the

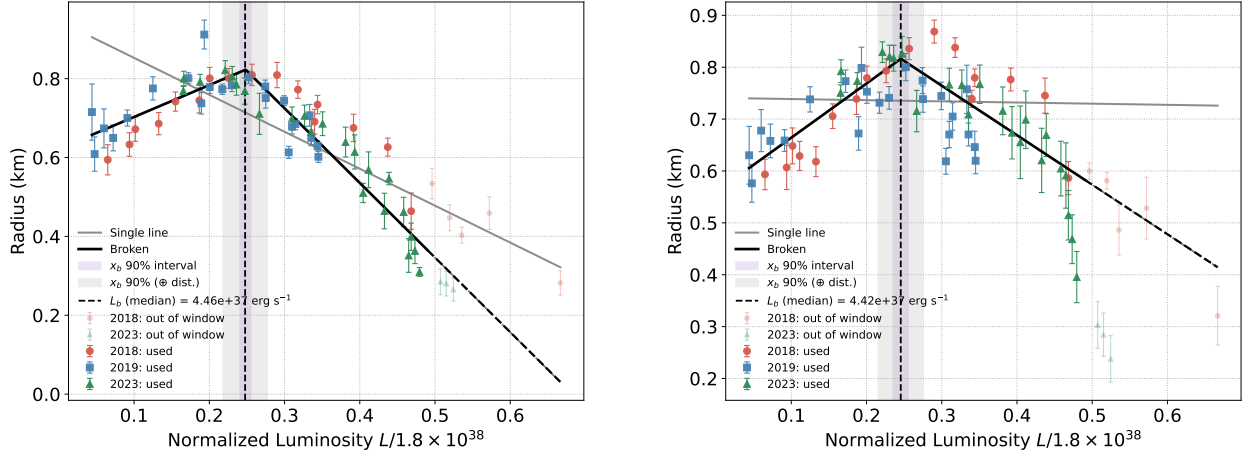


Figure 3. Broken–linear fit to *Radius* versus normalized luminosity $x = L/(1.8 \times 10^{38})$ with $x \leq 0.49$. Data points are color-coded by year; the solid curve represents the maximum-a-posteriori (MAP) broken–line model, and the vertical dashed line marks the break location. The gray and purple shaded bands show, respectively, the 90% credible intervals for x_b with and without the inclusion of distance uncertainty. **Left panel** (Insight–HXMT, frozen N_H): the break corresponds to $L_x = (4.46^{+0.53}_{-0.53}) \times 10^{37} \text{ erg s}^{-1}$. **Right panel** (Insight–HXMT, thawed N_H): the break is $L_x = (4.42^{+0.54}_{-0.54}) \times 10^{37} \text{ erg s}^{-1}$.

Table 1. Model comparison and break luminosity results for all datasets.

Group	Dataset	$\Delta \ln \mathcal{L}$	ΔAICc	ΔBIC	p_{LRT}	L_b, MAP	$L_b, 90\% \text{ CI}$	ΔL
		($10^{37} \text{ erg s}^{-1}$)	($10^{37} \text{ erg s}^{-1}$)	($10^{37} \text{ erg s}^{-1}$)		($10^{37} \text{ erg s}^{-1}$)	($10^{37} \text{ erg s}^{-1}$)	
Group 1	Insight–HXMT	364.49	724.48	720.72	$< 10^{-4}$	4.46	[3.93, 4.99]	+0.00
Group 2	Insight–HXMT (Thaw–NH)	130.08	255.67	251.88	$< 10^{-4}$	4.42	[3.88, 4.96]	-0.04
Group 3	Joint	77.21	149.47	147.32	$< 10^{-4}$	4.17	[3.91, 4.82]	-0.29
Group 4	Joint (cut 0.7–2 keV)	33.40	61.85	59.70	$< 10^{-4}$	5.33	[4.63, 6.07]	+0.87

NOTE—All tests favor the broken–line model (M_1) over the single–line model (M_0). The p –values from the LRT (Likelihood–Ratio Test) are reported as upper limits, since none of the simulations exceeded the observed $\Delta \ln \mathcal{L}$, indicating that the improvement is statistically significant. Overall, the break luminosities derived from the four datasets are consistent within the uncertainties. The column ΔL is computed relative to the best-fit break luminosity of Group 1. Note that for Group 4, the spectral parameters were obtained by excluding the 0.7–2 keV band, while the luminosities were still calculated following Case 2. As a result, the luminosities are systematically higher by about 10% compared to those derived in Case 1 (see Section 3.1). If a 10% systematic uncertainty is taken into account for Groups 3 and 4, the corresponding break luminosities become $L_b = 3.75$ [3.52, 4.34] and 4.80 [4.17, 5.46], respectively, which are consistent with those of Groups 1 and 2 within the uncertainties.

model adequately captures the spectral shape. In Group (b) (joint fits), the trends are consistent with those in Group (a), but for $L_X \gtrsim 8.8 \times 10^{37} \text{ erg s}^{-1}$, the reduced χ^2 increases from about 1.0 to 1.5. We find that adding an additional Gaussian iron-line component can reduce the reduced χ^2 , but this part does not affect the main results of this paper and is beyond the scope of discussion, so we do not investigate it further.

The first four panels of Figure 4 display the fitting results for the representative Group (a) data. The (a) panel of Figure 4 shows that the spectra of different outbursts observed with Insight–HXMT can be

well described by our model, and no significant differences are found at the same luminosity. Furthermore, We find that group (c), the narrowband fits (NICER only), which are consistent with those reported in Chhotaray et al. (2024), cannot constrain the spectral parameters very well. In group (c), all parameter values and their evolutionary trends diverge markedly, the `bbbodyrad` component drifts to a low-temperature, large-scale solution ($kT \sim 0.4$ keV, $R \sim 20$ km), while the other groups converge on a high-temperature, small-scale blackbody ($kT \sim 3$ keV, $R \sim 1$ km).

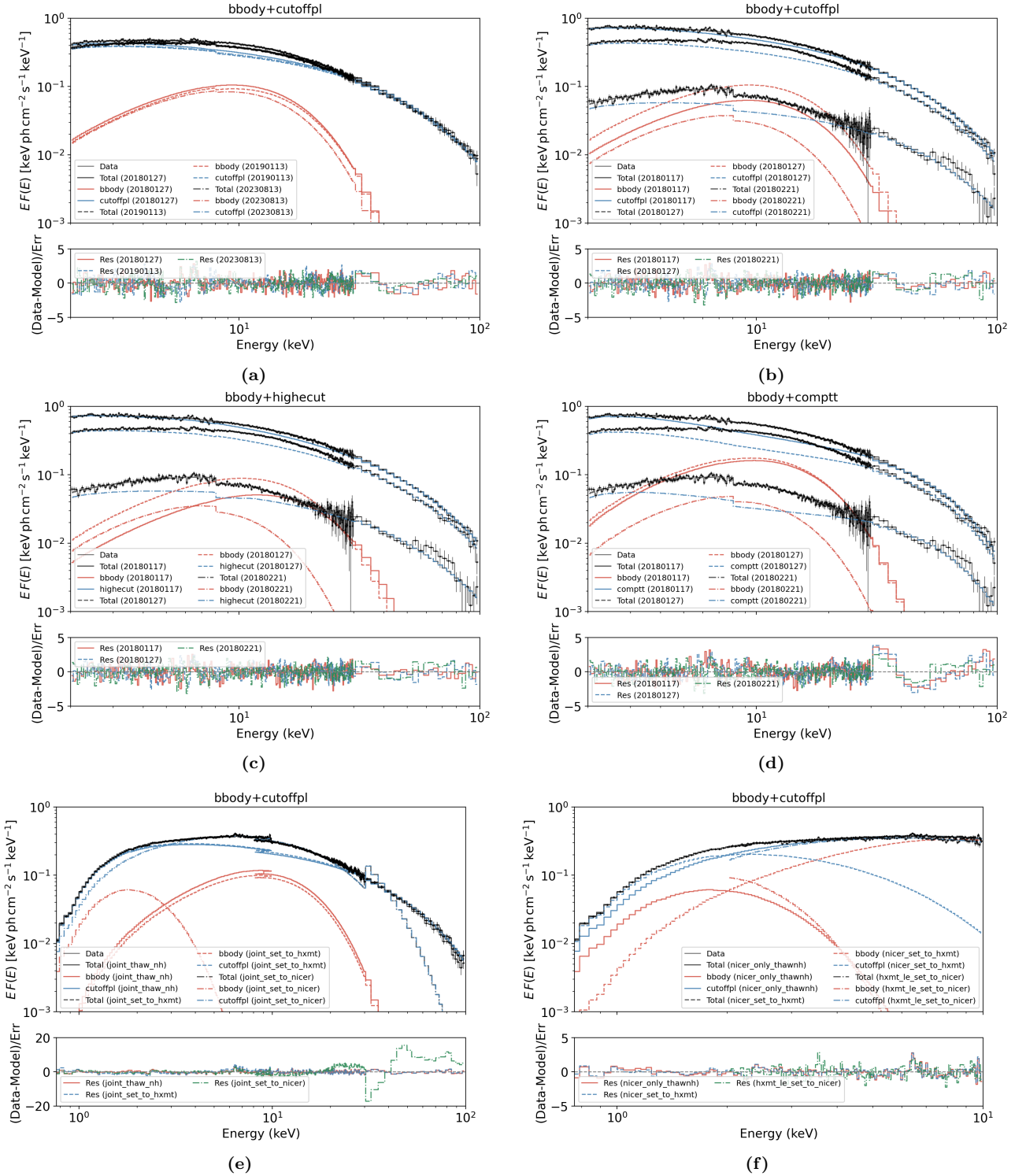


Figure 4. Panel (a): Comparison of spectral fits at similar luminosities from three observations in different outbursts, using Insight-HXMT data only. Panels (b)–(d): Spectral fits for three representative observations at luminosities below, around, and above L_t , respectively, obtained with different continuum models; the corresponding best-fit parameters are listed in Table 2. Panel (e): Joint spectral fitting of the 2018 February 02 observation over 0.7–100 keV with N_{H} free, comparing three cases: (1) a fully free joint fit; (2) a joint fit with the continuum fixed to the Insight-HXMT-only best fit in 2–100 keV; and (3) a joint fit with the continuum fixed to the NICER-only best fit in 0.7–10 keV. In cases (2) and (3), N_{H} , the normalization, and the cross-calibration constant are allowed to vary. Panel (f): Fits to the 2018 February 02 NICER and Insight-HXMT LE data with N_{H} free, comparing: (1) a free NICER-only fit in 0.7–10 keV; (2) a free Insight-HXMT LE-only fit in 2–10 keV with parameters initialized at the NICER best-fit values; and (3) a NICER-only fit initialized at the best-fit parameters from the fully free joint fit.

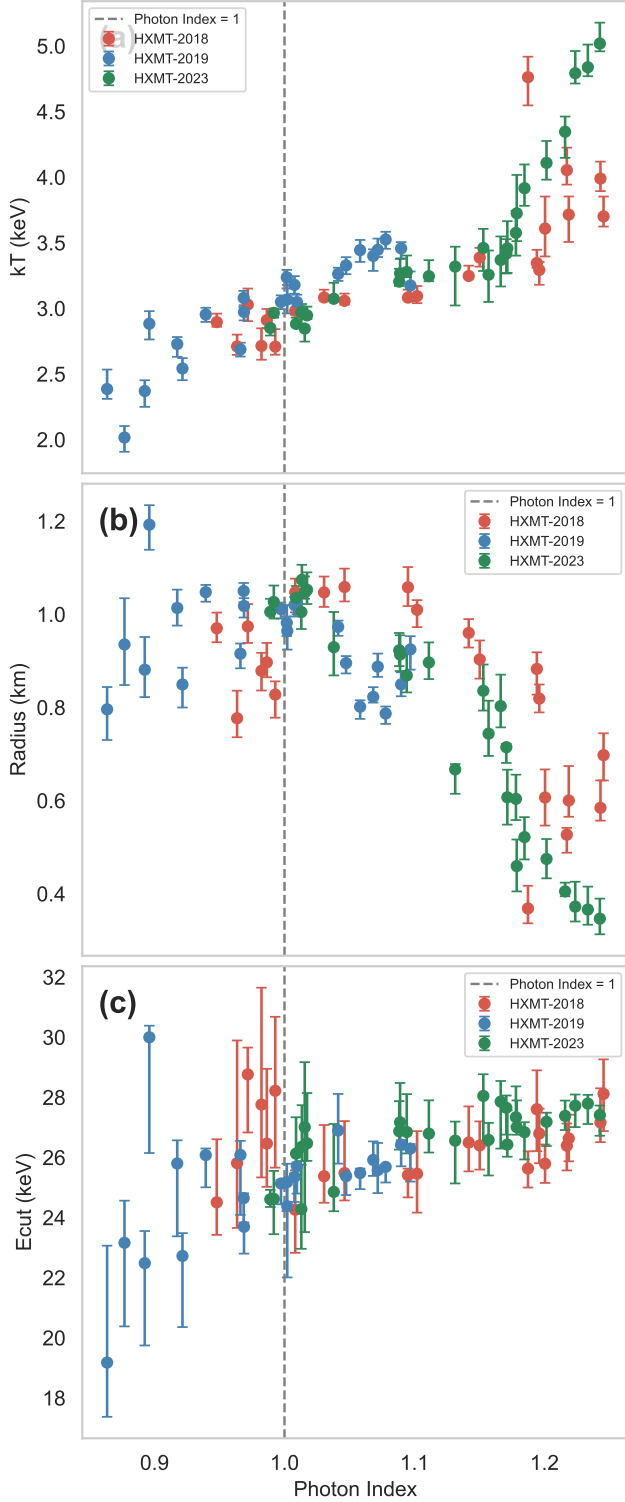


Figure 5. Correlation between model parameters and the photon index. The grey dashed line represents Photon Index = 1.0, corresponding to L_t .

We performed a restricted-fitting test on the 2018 February 02 observation. Prior to the joint fit over the 0.7–100 keV band, the continuum parameters were separately fixed to the best-fit values obtained from the Insight–HXMT (2–100 keV) and NICER (0.7–10 keV) single-instrument fits (see Figure 4(e); the free-fit results for the three instrumental configurations are summarized in Table 3). Fixing the continuum to the Insight–HXMT best-fit values yields results consistent with the fully free joint fit, whereas fixing it to the NICER best-fit values produces pronounced residual structures above ~ 20 keV, indicating that the spectral shape inferred from NICER is incompatible with the high-energy data.

We further examine the NICER results (see Figure 4(f)) and find that the continuum shape obtained from a free fit to the Insight–HXMT LE data in the 2–10 keV band is consistent with the NICER spectrum. However, when the initial parameter values of the NICER fit are set to those from the joint-fit, the resulting fit is clearly inconsistent with both the joint-fit and NICER-only results, indicating that model degeneracy alone is insufficient to account for the spectral bias introduced by narrow-band fitting. We therefore conclude that fitting with NICER data alone can intrinsically bias the inferred continuum and lead to nonphysical results.

In summary, although the spectral results of Chhotaray et al. (2024) provide supporting evidence for the outburst evolution of Swift J0243.6+6124, the parameters are not well constrained because of the limited bandwidth. We base our subsequent analysis primarily on the Insight–HXMT and joint-fit results.

3.3. Spectral Evolution in Sub-Eddington Regime

In the Insight–HXMT–only results (Figure 2(a)), we detect a high-temperature blackbody component with $kT \sim 3$ keV and radius $R \sim 1$ km, consistent with soft X-ray emission from a hotspot (Kong et al. 2020; Moshutukov & Tsygankov 2022). The blackbody radius was derived from the model normalization as

$$R_{\text{km}} = \sqrt{\text{Norm}_{\text{bb}}} D_{10}, \quad (1)$$

where $\text{Norm}_{\text{bb}} = R_{\text{km}}^2 / D_{10}^2$. Here R_{km} is the source radius in km, and D_{10} is the source distance in units of 10 kpc. For Swift J0243.6+6124, we adopt a distance of 5.2 kpc (Bailer-Jones et al. 2018), corresponding to $D_{10} = 0.52$. The joint fit yields consistent results. In both datasets, the blackbody radius–luminosity relation exhibits a clear break, where the correlation changes from positive to negative.

To quantitatively characterize this break, we modeled the radius–luminosity relation with a continuous

Table 2. Spectral Parameters for Three Observations

Component	Parameter	20180221 ($\sim 1.17 \times 10^{37}$ erg s $^{-1}$)			20180127 ($\sim 6.12 \times 10^{37}$ erg s $^{-1}$)			20180117 ($\sim 8.43 \times 10^{37}$ erg s $^{-1}$)		
		Model 1	Model 2	Model 3	Model 1	Model 2	Model 3	Model 1	Model 2	Model 3
Tbabs	N_{H} (10 22 cm $^{-2}$)	1.08 $^{+0.09}_{-0.04}$	0.92 $^{+0.20}_{-0.19}$	2.02 $^{+0.04}_{-0.04}$	0.73 $^{+0.04}_{-0.04}$	0.69 $^{+0.20}_{-0.24}$	1.64 $^{+0.01}_{-0.01}$	0.63 $^{+0.14}_{-0.02}$	0.59 $^{+0.24}_{-0.14}$	1.81 $^{+0.25}_{-0.09}$
bbodyrad	kT (keV)	2.71 $^{+0.14}_{-0.06}$	2.75 $^{+0.12}_{-0.12}$	2.89 $^{+0.05}_{-0.06}$	3.29 $^{+0.08}_{-0.08}$	3.28 $^{+0.06}_{-0.03}$	3.20 $^{+0.03}_{-0.03}$	3.24 $^{+0.25}_{-0.22}$	3.24 $^{+0.06}_{-0.23}$	3.41 $^{+0.04}_{-0.03}$
bbodyrad	norm	1.30 $^{+0.06}_{-0.19}$	1.18 $^{+0.08}_{-0.20}$	1.41 $^{+0.02}_{-0.02}$	2.02 $^{+0.12}_{-0.06}$	2.03 $^{+0.12}_{-0.16}$	3.60 $^{+0.11}_{-0.07}$	1.27 $^{+0.11}_{-0.16}$	1.28 $^{+0.25}_{-0.11}$	2.85 $^{+0.21}_{-0.32}$
cutoffpl	Γ	0.97 $^{+0.08}_{-0.04}$	1.10 $^{+0.02}_{-0.01}$	1.14 $^{+0.03}_{-0.01}$
cutoffpl	E_{cut} (keV)	25.9 $^{+2.6}_{-0.7}$	25.3 $^{+1.0}_{-0.3}$	24.7 $^{+0.8}_{-0.3}$
cutoffpl	norm	0.07 $^{+0.01}_{-0.01}$	0.58 $^{+0.02}_{-0.01}$	1.00 $^{+0.04}_{-0.01}$
highecut	E_{break} (keV)	...	4.8 $^{+2.3}_{-1.0}$	2.3 $^{+0.3}_{-0.7}$	2.4 $^{+0.3}_{-0.8}$...
highecut	E_{fold} (keV)	...	26.5 $^{+1.0}_{-2.1}$	25.3 $^{+0.9}_{-1.1}$	24.7 $^{+1.2}_{-1.0}$...
powerlaw	Γ	...	1.01 $^{+0.06}_{-0.07}$	1.10 $^{+0.03}_{-0.03}$	1.14 $^{+0.03}_{-0.03}$...
powerlaw	norm	...	0.06 $^{+0.01}_{-0.01}$	0.53 $^{+0.04}_{-0.03}$	0.90 $^{+0.06}_{-0.05}$...
CompTT	T_0 (keV)	0.06 $^{+0.01}_{-0.01}$	0.09 $^{+0.01}_{-0.01}$	0.25 $^{+0.02}_{-0.02}$
CompTT	kT (keV)	12.4 $^{+0.1}_{-0.1}$	12.1 $^{+0.1}_{-0.1}$	12.0 $^{+0.1}_{-0.2}$
CompTT	τ	3.74 $^{+0.06}_{-0.06}$	3.38 $^{+0.01}_{-0.01}$	3.18 $^{+0.06}_{-0.07}$
CompTT	norm (10 $^{-2}$)	5.3 $^{+0.2}_{-0.2}$	34.5 $^{+0.9}_{-1.1}$	32.2 $^{+2.0}_{-1.3}$
	$\chi^2_{\mathrm{red}}/\mathrm{dof}$	0.89/309	0.89/308	0.92/308	0.90/309	0.90/308	1.14/308	0.91/309	0.91/308	1.18/308

NOTE— Uncertainties are quoted at the 90% confidence level and are derived from MCMC chains of length 20 000. For each observation, three spectral models are applied: Model 1: `tbabs` \times (`bbodyrad` + `cutoffpl`); Model 2: `tbabs` \times (`bbodyrad` + `highecut` \times `powerlaw`); Model 3: `tbabs` \times (`bbodyrad` + `CompTT`). The energy range used for spectral fitting is 2–100 keV.

broken–linear function of the form

$$y = \begin{cases} y_b + m_1(x - x_b), & x \leq x_b, \\ y_b + m_2(x - x_b), & x > x_b, \end{cases} \quad (2)$$

where m_1 and m_2 denote the slopes below and above the break luminosity x_b , and y_b is the model value at the break point. We excluded data points above 8.8×10^{37} erg s $^{-1}$ (2–150 keV, 5.2 kpc), where an additional transition has been reported (Kong et al. 2020; Mushtukov & Tsygankov 2022).

We use uniform box priors to constrain the parameters of the broken–line model, where $x_b \in [3 \times 10^{37}, 8 \times 10^{37}]$ erg s $^{-1}$, $y_b \in [-10^3, 10^3]$, and $m_1, m_2 \in [-10^3, 10^3]$. We use emcee with 40 walkers, a burn–in of 2000 steps, and 20 000 production steps. We report the MAP (Maximum A Posteriori) with 90% credible intervals for all parameters. We incorporate the distance uncertainty as a systematic component of the final error budget (with a distance of 5.2 $^{+0.3}_{-0.3}$ kpc). Figure 3 shows the final uncertainty bands obtained with and without including the distance uncertainty, demonstrating that the uncertainty introduced by the distance error is non-negligible.

For comparison, we also fit a single–line model M_0 described as $y = a + b(x - x_0)$, where $x_0 = \langle x \rangle$, and compare it with the continuous broken–line model M_1 . We center the single–line model at $x_0 = \langle x \rangle$. To test whether

introducing a break (i.e. two additional free parameters) is statistically warranted, we compute for each dataset the differences $\Delta \ln \mathcal{L}$, $\Delta \mathrm{AICc}$, and $\Delta \mathrm{BIC}$, where $\Delta \ln \mathcal{L}$ quantifies the improvement in log-likelihood and $\Delta \mathrm{AICc}$ and $\Delta \mathrm{BIC}$ are the corresponding changes in the corrected Akaike and Bayesian information criteria between the broken and single-power-law models. In addition, we perform a Likelihood–Ratio Test with 10 000 bootstrap iterations under M_0 , simulating $y_i^{(\mathrm{sim})} \sim \mathcal{N}[\mu_0(x_i), \sigma_i^2]$ using the M_0 MLE (Maximum Likelihood Estimate), refitting M_0 and M_1 to each realization, and forming the empirical null distribution of $\Delta \ln \mathcal{L}$.

We conducted tests on four datasets, with detailed results presented in Table 1. For clarity, we present the fitting results of Group 1 and Group 2 in Figure 3, and the corresponding corner plots are shown in Figure 8 of Appendix A. The results show that the broken–line model performs better across all datasets, as all $\Delta \mathrm{AICc}$ and $\Delta \mathrm{BIC}$ values exceed 10, and no single LRT (Likelihood–Ratio Test) simulation exceeds the observed $\Delta \ln \mathcal{L}$. Comparing four datasets shows that allowing N_{H} to vary has little impact on the break luminosity, whereas including the 0.7–2 keV data may slightly shift the transition luminosity toward lower value, indicating that the break is robust (The transition luminosities derived from the four datasets are consistent within the uncertainties at the 90% confidence level, see Table 1). We also examined the evolution of the constant model

Table 3. Spectral Parameters of the 2018 February 02

Component	Parameter	Joint	NICER	Insight-HXMT
constant	C_1	1.0 (frozen)	—	1.0 (frozen)
constant	C_2	$0.89^{+0.010}_{-0.010}$	—	$0.97^{+0.014}_{-0.0070}$
constant	C_3	$0.83^{+0.026}_{-0.025}$	—	$0.91^{+0.018}_{-0.023}$
Tbabs	$N_H (10^{22} \text{ cm}^{-2})$	$1.1^{+0.012}_{-0.012}$	$0.93^{+0.018}_{-0.025}$	$0.96^{+0.15}_{-0.18}$
bbbodyrad	$kT (\text{keV})$	$3.0^{+0.059}_{-0.058}$	$0.48^{+0.026}_{-0.022}$	$3.0^{+0.026}_{-0.066}$
bbbodyrad	norm	$2.9^{+0.16}_{-0.15}$	590^{+65}_{-110}	$2.5^{+0.16}_{-0.14}$
cutoffpl	Γ	$1.0^{+0.018}_{-0.018}$	$0.23^{+0.055}_{-0.071}$	$1.0^{+0.032}_{-0.024}$
cutoffpl	$E_{\text{cut}} (\text{keV})$	$25^{+1.0}_{-0.98}$	$8.3^{+0.63}_{-0.74}$	$25^{+1.1}_{-0.78}$
cutoffpl	norm	$0.35^{+0.0059}_{-0.0058}$	$0.20^{+0.012}_{-0.012}$	$0.36^{+0.022}_{-0.017}$
	$\chi^2_{\text{red}}/\text{dof}$	0.68/350	0.61/141	0.82/332

NOTE— Spectra are fitted with model: $\text{TBabs} \times (\text{bbbodyrad} + \text{cutoffpl})$. Constants are included only when multiple data groups are jointly fitted.

parameter and found no systematic variation near the transition(see Figure 10 in Appendix A).

Taken together, these results confirm that a genuine break exists in the parameter evolution, corresponding to a new transition luminosity of $L_b = 4.46^{+0.53}_{-0.53} \times 10^{37} \text{ erg s}^{-1}$ (from Group 1). For consistency with previous studies(Kong et al. 2020; Wang et al. 2020), we adopt the transition luminosity, $L_t \sim 4.5 \times 10^{37} \text{ erg s}^{-1}$, measured in Group 1 throughout this work.

We selected three observations just below (20180221), near (20180127), and above (20180117) L_t to illustrate the spectral evolution. The spectral comparison across L_t is shown in Figure 4 and Table 2, and the corner plots of the model parameters are presented in Figure 9 of Appendix A (Taking the results of Group 1 as an example). For all three spectral models, the evolution of the blackbody component is consistent, showing an increase followed by a decrease as the luminosity rises, which further supports the presence of a break luminosity.

Together, Figures 2(a) and 2(b) show that across L_t the blackbody temperature steadily increases; the radius–luminosity correlation reverses from positive to negative; Γ evolves from nearly constant to positively correlated with luminosity; and the evolution of E_{cut} slows. In Figure 5, the grey dashed line marks the photon index around L_t . We observe that on either side of L_t , both the blackbody area (Norm_{bb}) and the cutoff energy (E_{cut}) exhibit breaks in their correlation with the photon index, and the evolution of E_{cut} as a function of Γ becomes noticeably slower. Overall, E_{cut} is positively correlated with Γ , which is consistent with the results reported by Reig & Nespoli (2013) for other sources.

Our results also reveal differences between outbursts. As shown in Figure 2(a), although the overall spectral evolution during the decay phases is broadly similar, the 2018 giant outburst exhibits systematic deviations. With increasing luminosity, the blackbody temperature evolution of the giant outburst diverges from that of the normal outbursts, and its photon index is systematically higher, indicating a softer spectrum. These differences are most apparent when viewed in the context of the full evolutionary sequence and likely reflect distinct accretion environments during the giant outburst.

Giant (Type II) outbursts are commonly associated with enhanced mass transfer from a perturbed Be-star circumstellar disk, whereas normal (Type I) outbursts are typically triggered by increased mass transfer near periastron, naturally leading to different accretion environments(Reig 2011). In addition, the soft excess observed during the giant outburst may be related to disk-structure effects: under supercritical accretion, strong radiation pressure near the inner disk can drive optically thick outflows (Tao et al. 2019; Doroshenko et al. 2020), part of which may be recaptured as the accretion rate declines, producing additional soft X-ray emission. Furthermore, the bifurcation in the blackbody temperature–luminosity relation at high L_X between the 2018 and 2023 outbursts may arise because the 2023 outburst peaked at a luminosity close to $L_1 \sim 8.8 \times 10^{37} \text{ erg s}^{-1}$, and therefore did not enter the transition associated with the Zone II accretion regime (Kong et al. 2020).

4. DISCUSSION

We performed a detailed spectral analysis of the decay phases of Swift J0243.6+6124 observed by Insight-HXMT and NICER during three outbursts. The evolution of the spectral parameters reveals a clear transition at $L_t \sim 4.5 \times 10^{37} \text{ erg s}^{-1}$, constrained by the Insight-HXMT and joint-fit spectra, as the NICER-only fits are limited by their narrow energy coverage. This transition can be observed in multiple alternative models (see Table 2) and is robust under different fitting conditions (see Table 1). To clearly illustrate the position of L_t among the known transitions, we list all transition luminosities identified to date across six orders of magnitude in accretion evolution of Swift J0243.6+6124 ($L_X \sim 1.0 \times 10^{34}$ to $> 1 \times 10^{39} \text{ erg s}^{-1}$): $L_1 \sim 7 \times 10^{36} \text{ erg s}^{-1}$ (Serim et al. 2023), the newly discovered $L_t \sim 4.5 \times 10^{37} \text{ erg s}^{-1}$, and three higher-luminosity transitions at $L_3 \sim 8.8 \times 10^{37}$, $L_4 \sim 2.8 \times 10^{38}$ (Doroshenko et al. 2020; Kong et al. 2020), and $L_5 \sim 4.5 \times 10^{38} \text{ erg s}^{-1}$ (Wang et al. 2020)(All luminosities have been recalculated assuming a distance of 5.2 kpc.).

Among these luminosities, only the transitions at L_3 and L_4 currently show both spectral and timing signatures. Around L_1 and L_5 , detailed spectral studies are lacking, and transitions are indicated only by timing signatures. The transition at L_t is identified from spectral signatures, and its timing study is currently in progress. We emphasize that observing so many transitions in a single source is unprecedented (most sources show only one or two)(Reig & Nespoli 2013)).

Additionally, the luminosity at which L_t appears is particularly peculiar. Insight–HXMT monitoring has established that the critical luminosity of Swift J0243.6+6124 occurs at a higher value (L_4), consistent with the 146 keV CRSF detection (Kong et al. 2020, 2022). If L_t instead corresponds to a subcritical transition, its luminosity would be one to two orders of magnitude higher than in other accretion-powered X-ray pulsars (Reig & Nespoli (2013), e.g., EXO 2030+375, KS 1947+300, Swift J1626.6–5156). This indicates that L_t may represents a previously unrecognized subcritical transition.

The physics in the subcritical regime remains uncertain and several mechanisms have been proposed to explain the emergence of transition luminosities below the critical value(Basko & Sunyaev 1975; Langer & Rappaport 1982; Becker et al. 2012; Postnov et al. 2015; Becker & Wolff 2022). A possible association is between L_t and the Coulomb luminosity, L_{Coul} . At very low luminosities ($L_X \lesssim 10^{34–35} \text{ erg s}^{-1}$), the gas-mediated shock forms close to the neutron-star surface and inflowing matter decelerates almost entirely at the stellar surface. As L_X rises toward L_{Coul} , the emission height increases, the shock front lifts above the surface, and Coulomb interactions complete the final deceleration. The minimum luminosity at which Coulomb drag can halt the inflow is estimated as

$$L_{\text{Coul}} = 1.17 \times 10^{37} \text{ erg s}^{-1} \left(\frac{\Lambda}{0.1} \right)^{-7/12} \left(\frac{\tau_*}{20} \right)^{7/12} \left(\frac{M_*}{1.4 M_\odot} \right)^{11/8} \times \left(\frac{R_*}{10 \text{ km}} \right)^{-13/24} \left(\frac{B_*}{10^{12} \text{ G}} \right)^{-1/3} \quad (3)$$

where Λ is the accretion-geometry parameter, τ_* the Thomson optical depth parameter, and M_* , R_* , and B_* are the neutron star mass, radius, and surface magnetic field, respectively(Langer & Rappaport 1982; Becker et al. 2012).

If we adopt typical neutron star parameters ($M_* = 1.4 M_\odot$, $R_* = 10 \text{ km}$) and set $\Lambda = 0.1$ and $\tau_* = 20$, then the observed $L_t \sim 4.5 \times 10^{37} \text{ erg s}^{-1}$ would imply an implausibly low surface magnetic field of $B \sim$

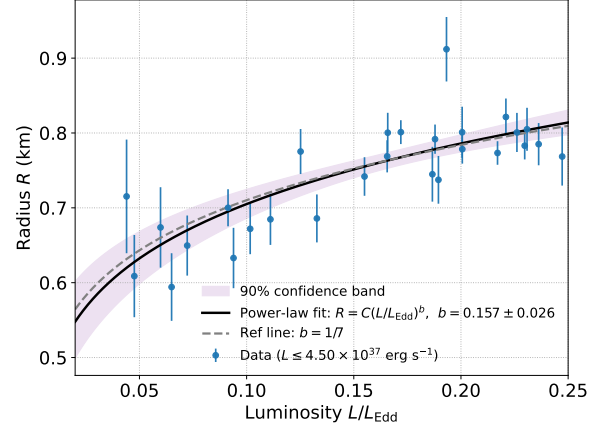


Figure 6. Power-law fit to the radius–luminosity relation using $R = C(L/L_{\text{Edd}})^b$ for the Insight–HXMT-only sample. The fit is performed using only data with $L \leq 4.5 \times 10^{37} \text{ erg s}^{-1}$. The purple shaded band marks the 90% credible interval around the posterior median fit. For visual comparison, a gray dashed reference with fixed $b = 1/7$ is overplotted.

$1.7 \times 10^{10} \text{ G}$. Even under the most extreme assumptions in the L_{Coul} formula—namely $M_* = 3 M_\odot$, $R_* = 15 \text{ km}$, and $\Lambda = 0.66$, matching L_t would require a surface field strength of order 10^{11} G , far below previous estimates (Tsygankov et al. 2018; Doroshenko et al. 2020; Kong et al. 2020, 2022; Serim et al. 2023). These calculations strongly suggest that L_t is unlikely to correspond to L_{Coul} .

Theoretical model by Becker et al. (2012) based on a dipole magnetic field predict two transition luminosities, L_{Coul} and L_{crit} , neither of which matches the observed L_t . Moreover, Swift J0243.6+6124 exhibits as many as five distinct transitions, far exceeding theoretical expectations. We propose that the presence of multipolar magnetic fields may be the underlying cause of L_t and other transitions observed in this source.

A combination of dipole and quadrupole fields naturally produces asymmetric polar-cap field strengths: one pole is compressed and intensified(strong pole), the other is extended and weakened(weak pole), and if the quadrupole exceeds the dipole locally, the hotspot may become an annular ring(Gralla et al. 2017; Lockhart et al. 2019). This geometry can give rise to distinct spectral transitions at each pole. In this source, the growth of the column and the emergence of sidewall emission provide an opportunity to view radiation from both poles. Moreover, the existence of multipolar magnetic fields can alter the magnetic field configuration, making the detection of emission from both poles a plausible scenario(Poutanen et al. 2024).

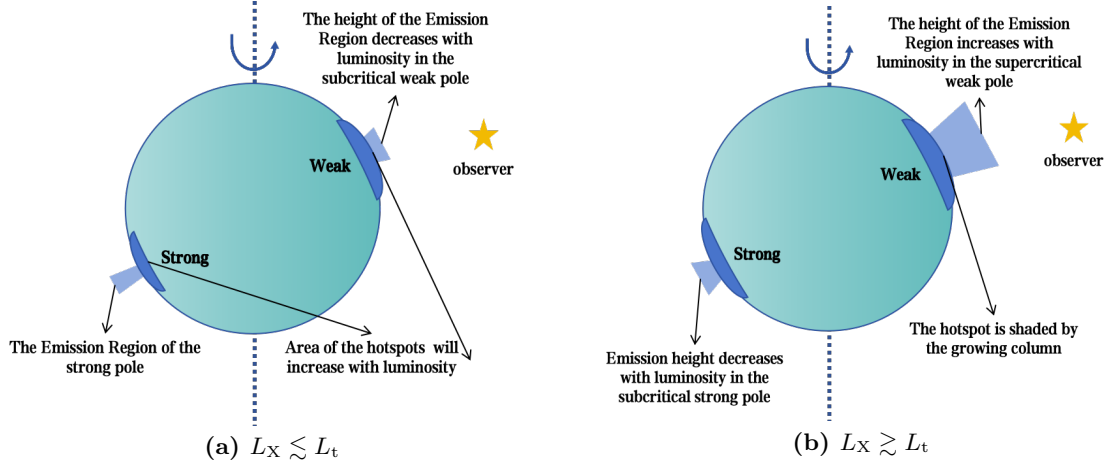


Figure 7. Sketch of the two zones defined in this paper during the sub-Eddington regime of Swift J0243.6+6124. (a) for $L_x \lesssim L_t$, the accretion column at the strong magnetic pole is formed, the emission height of the subcritical weak-pole column decreases with luminosity, and the blackbody radius at the polar cap region increases with luminosity; (b) for $L_x \gtrsim L_t$, the weak magnetic pole enters the supercritical regime, where the rapidly growing accretion column gradually shades the polar cap region, leading to a decrease in the blackbody radius. The variation of the emission height near the critical luminosity follows the framework discussed by Becker et al. (2012).

Under such a magnetic-field configuration, in which the two magnetic poles have different field strengths, the two poles may reach the critical regime at different times or luminosities rather than simultaneously, multiple spectral transitions can naturally arise. We can reconsider the possibility of L_t as the critical luminosity of a certain magnetic pole.

Before L_t , a possible spectral hardening is hinted at by comparing the NuSTAR photon index (~ 1.21 at relatively low luminosity; Table 2 in Tao et al. 2019, OBSID 90401308002) with our below- L_t value (~ 0.9). Thus, the spectrum around L_t most likely follows a hardening–plateau–softening sequence. The hardening and softening can be interpreted by the change of emission height across the critical luminosity, while the plateau represents the transition between the two regimes (Postnov et al. 2015). We therefore suggest that L_t may represent a critical luminosity, corresponding to a magnetic field strength of $B_S \sim 2.8 \times 10^{12}$ G, estimated by substituting typical neutron star parameters into the critical-luminosity formula:

$$L_{\text{crit}} \simeq 1.5 \times 10^{37} B_{12}^{16/15} \text{ erg s}^{-1}, \quad (4)$$

where B_{12} is the surface magnetic field in units of 10^{12} G (Becker et al. 2012).

The previously detected 146 keV cyclotron resonance scattering feature (CRSF) implies the presence of a strong magnetic field near the neutron-star surface, with $B_N \sim 1.6 \times 10^{13}$ G (Kong et al. 2022). When combined with the weaker surface field inferred from the transition luminosity, $B_S \sim 2.8 \times 10^{12}$ G, this naturally points to an asymmetric magnetic-field configuration between the

two magnetic poles. In Appendix B, we derive the polar magnetic-field strengths expected from an axisymmetric superposition of dipole and quadrupole components. Substituting the above field estimates into these expressions, we find that reproducing such a two-pole asymmetry requires dipole and quadrupole field strengths of 6.6×10^{12} G and 9.4×10^{12} G, respectively, corresponding to a quadrupole-to-dipole ratio of $q \simeq 1.4$. (After considering the uncertainties of transition luminosity and CRSF line, the ratio is $q = 1.42^{+0.06}_{-0.06}$, see Appendix B.)

Under this magnetic configuration, and further accounting for the measurement uncertainty of the CRSF energy (146^{+3}_{-4} keV) (Kong et al. 2022), the magnetic field strength at the stronger pole is $B_N = (1.57 \pm 0.04) \times 10^{13}$ G, which implies a critical luminosity of $L_{\text{crit}} = (2.83 \pm 0.08) \times 10^{38}$ erg s $^{-1}$ (using equation 4). This value is consistent with the observed $L_4 \sim 2.8 \times 10^{38}$ erg s $^{-1}$ (Kong et al. 2020), demonstrating that such a magnetic-field configuration can naturally reproduce the observed transition luminosity.

It is worth noting that when the distance from the star increases to ~ 300 km (comparable to the magnetospheric radius at high accretion rates for this source (Doroshenko et al. 2020)), the radial magnetic fields at the two poles have already decayed to nearly equal values, $\simeq 2.2 \times 10^8$ G. This is equivalent to the field produced at the same radius by a neutron star with a purely dipolar surface polar field of 6.6×10^{12} G (see Appendix B for the detailed derivation). The magnitude of this effective dipolar field is consistent with the dipole component inferred from other methods, a few

$\times 10^{12}$ G (Tsygankov et al. 2018; Doroshenko et al. 2020; Bykov et al. 2022; Serim et al. 2023; Inoue et al. 2023), while the presence of a quadrupolar component allows the surface field at one pole to exceed 10^{13} G (Wilson-Hodge et al. 2018; Zhang et al. 2019; Kong et al. 2020, 2022), thereby reconciling the apparent discrepancies among different magnetic-field estimates.

In addition, when the quadrupole-to-dipole ratio reaches $q \sim 1.4$, a ring-like geometry is expected to form around the weaker magnetic pole (Lockhart et al. 2019), which may cause the evolution of this source to differ from that of typical accreting X-ray pulsars, potentially allow it to reach higher luminosities and weaken the CRSF line. In particular, such a ring geometry can increase the effective length l_0 of the accretion-channel cross-section, thereby enhancing the ratio l_0/d_0 (where d_0 is the thickness of the accretion column) and consequently raising the maximum attainable luminosity (see Mushtukov et al. 2015b, their Eq. 10).

Although a local magnetic field of $B_S \sim 2.8 \times 10^{12}$ G would place the fundamental cyclotron resonance scattering feature (CRSF) within the Insight-HXMT/NuSTAR band, the detectability of such a feature depends sensitively on the radiative-transfer conditions rather than on the field strength alone.

Monte Carlo calculations show that the depth and width of CRSFs vary strongly with the line-forming geometry, optical depth, and viewing angle (Schönherr et al. 2007). In particular, the introduction of a quadrupole component leads to larger magnetic-field gradients at the polar region, and the quadrupole-to-dipole ratio of ~ 1.4 inferred in this work implies an extended, possibly ring-like, weak-pole region (Lockhart et al. 2019). In such a geometry, the observed spectrum originates from a range of emission heights and locations, naturally broadening the CRSF and potentially rendering the CRSF undetectable (Schönherr et al. 2007; Nishimura 2014). In addition, multi-zone photon spawning and the angular dependence of resonant absorption further reduce the line contrast in the continuum (Schönherr et al. 2007).

Turning back to the main transition of the blackbody radius, the photons contributing to this component mainly originate from the spectral region below ~ 15 keV. Their physical origin remains debated, but it is generally accepted that the softer X-ray photons are primarily produced in the vicinity of the neutron-star surface, either from the polar-cap region or the base of the accretion column (Becker & Wolff 2007, 2022). Observationally, the inferred blackbody emitting region has an effective radius of order ~ 1 km, and phase-resolved spectroscopy shows a clear modulation of the blackbody

parameters with pulse phase, supporting an origin close to the stellar surface (Jaisawal et al. 2018; Kong et al. 2020, 2022). Although a fully self-consistent physical model is still lacking, the blackbody component can be reasonably attributed to emission from the vicinity of the polar caps.

Under a dipolar magnetic-field assumption, the size of the polar-cap region can be estimated from the Alfvén radius R_A as

$$R_{\text{cap}} \lesssim R_{\text{NS}} \sqrt{\frac{R_{\text{NS}}}{R_A}}, \quad (5)$$

$$R_A = \xi \mu^{4/7} (2\dot{M})^{-2/7} (2GM_{\text{NS}})^{-1/7}, \quad \mu = B_0 R_{\text{NS}}^3, \quad (6)$$

with $\xi \simeq 1$ (Lamb et al. 1973; Sokolova-Lapa et al. 2021). Equations (5)–(6) imply $R_{\text{cap}} \propto \dot{M}^{1/7}$. We find that the radius–luminosity relation below L_t follows this trend well. By fitting the pre- L_t rise with $R = C(L/L_{\text{Edd}})^b$, we obtain $b \simeq 1/7$, indicating an accretion-rate dependence consistent with that expected for dipolar magnetic fields, even in the possible presence of multipolar components (see Figure 6). Above the supercritical luminosity, the enhancement of the accretion column may lead to stronger reprocessing of soft X-ray photons from the polar-cap region, thereby causing an apparent decrease of the inferred radius, resembling a self-occultation effect. Assuming that L_t corresponds to the critical luminosity of the weaker magnetic pole, we illustrate in Figure 7 the schematic geometry of both magnetic poles around L_t , highlighting the obscuration of the polar cap region by the accretion column.

We also considered alternative possibilities. Multiple lines of evidence suggest that the transition from a gas-pressure-dominated disk to a radiation-pressure-dominated disk occurs at much higher luminosities, above the Eddington limit (Doroshenko et al. 2020). The newly identified transition luminosity is well below the Eddington luminosity and is therefore unlikely to be driven by a structural change of the accretion disk. Moreover, changes in the beaming pattern are generally associated with the onset of the supercritical accretion regime and are expected to be accompanied by significant variations in the pulse profiles (Becker et al. 2012; Kong et al. 2020). If L_t indeed corresponds to the critical luminosity of the weaker magnetic pole, this scenario can be further examined through pulse-profile evolution.

One plausible scenario is a change in the dominant type of seed photons: at low accretion rates blackbody emission may dominate, whereas at higher rates bremsstrahlung becomes important, and the interplay

between these photon sources can produce a characteristic luminosity at which the spectral evolution changes (Becker & Wolff 2022). This model further predicts a potential spectral hardening process, suggesting that the spectrum becomes harder when bremsstrahlung dominates compared to the regime in which blackbody emission is dominant. However, above L_t we observe spectral softening, with a hardening trend emerging only after L_3 . If L_t indeed arises from a change in the seed-photon population, then updated physical models and parameter evolution over a broader luminosity range will be required to verify this interpretation.

5. CONCLUSIONS

We have carried out a detailed broadband spectral analysis of Insight–HXMT observations of Swift J0243.6+6124 in its sub-Eddington regime, complemented by joint fits with contemporaneous NICER data. These combined results reveal a new transition at $L_t \sim 4.5 \times 10^{37} \text{ erg s}^{-1}$ within the sub-Eddington regime, indicating that this source exhibits unprecedented spectral complexity with at least five intrinsic transition luminosities. This behavior suggests a fascinating multipolar magnetic geometry, in which a weak pole ($B_{\text{weak}} \sim 2.8 \times 10^{12} \text{ G}$) and a strong pole ($B_{\text{strong}} \sim 1.6 \times 10^{13} \text{ G}$ (Kong et al. 2022)) alternately dominate the emission. Furthermore, we found that to give such a magnetic field configuration, both dipole and quadrupole components are comparable. The non-dipole field is equivalent to a pure dipole magnetic field of $\sim 6.6 \times 10^{12} \text{ G}$ on the scale of the magnetospheric radius.

¹ This work made primary use of data from the Insight–HXMT mission, a project funded by the China National Space Administration (CNSA) and the Chinese Academy of Sciences (CAS). We thank the High Energy Astrophysics Science Archive Research Center (HEASARC) at NASA’s Goddard Space Flight Center for providing the data. This work is supported by the China’s Space Origins Exploration Programthe, National Key R&D Program of China (2021YFA0718500) and the National Natural Science Foundation of China (NSFC) under Grants No. 12025301 and 12333007. It is also partially supported by the International Partnership Program of the Chinese Academy of Sciences (Grant No. 113111KYSB20190020). Pengju Wang is grateful for the financial support provided by the Sino-German (CSC-DAAD) Postdoc Scholarship Program (57678375)

APPENDIX

A. SUPPLEMENTARY FIGURES

This Appendix presents supplementary figures supporting the MCMC-based spectral analysis, including corner plots for the grouped fits (Figure 8), posterior-distribution comparisons for representative observations around L_t (Figure 9), and the luminosity dependence of the cross-calibration constants (Figure 10).

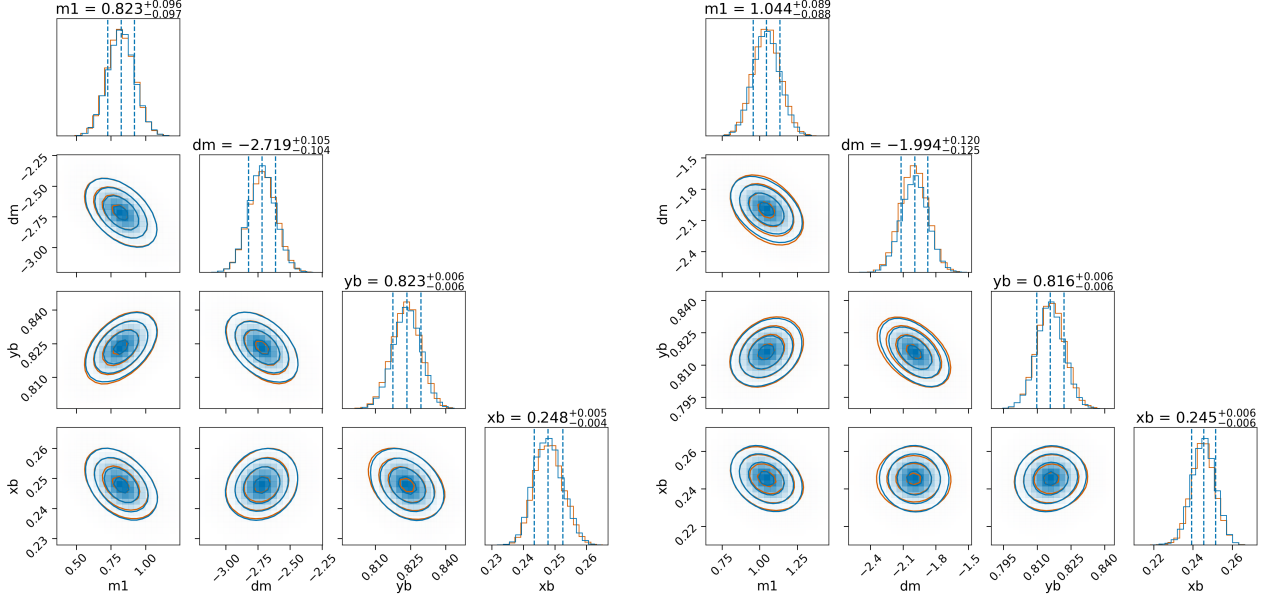


Figure 8. The corner plots for Group 1 and Group 2 in Table 1 are shown. Since m_2 is parameterized through $m_1 + \Delta m$, the corresponding parameter appearing in the plots is Δm .

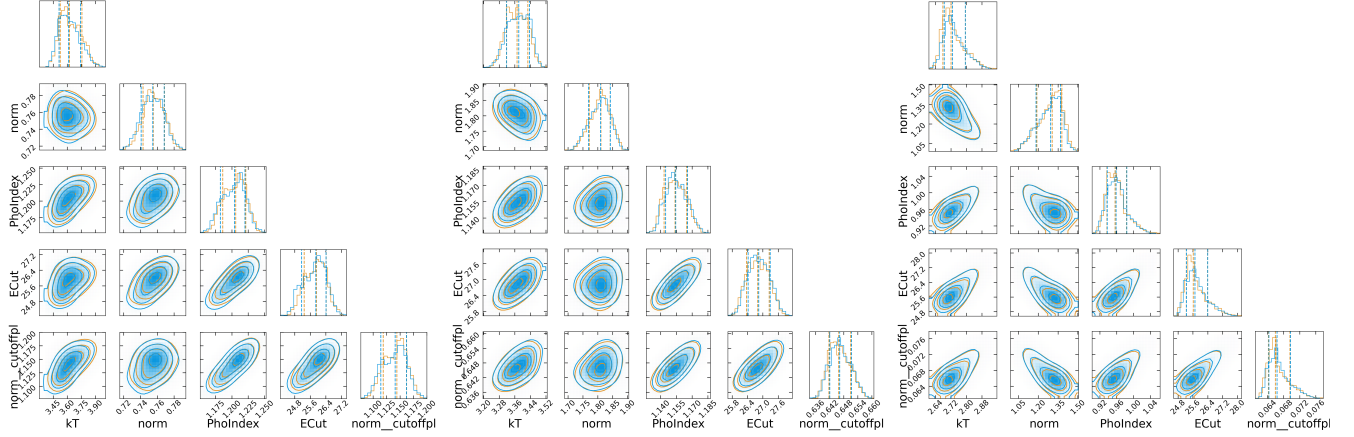


Figure 9. From left to right are the one- and two-dimensional projections of the posterior probability distributions for the three observations with luminosities above L_t , around L_t , and below L_t , respectively. These three observations correspond to those shown in the right panel of Figure 4: 2018-01-17, 2018-01-27, and 2018-02-21, with luminosities of 8.43×10^{37} erg s $^{-1}$, 6.12×10^{37} erg s $^{-1}$, and 1.17×10^{37} erg s $^{-1}$, respectively. The contours represent the 0.16, 0.50, and 0.84 quantiles obtained from the MCMC analysis of each free spectral parameter. To assess the convergence of the sampling chains, we compare the projections of the posterior distributions derived from the first half (orange) and the second half (blue) of the chains.

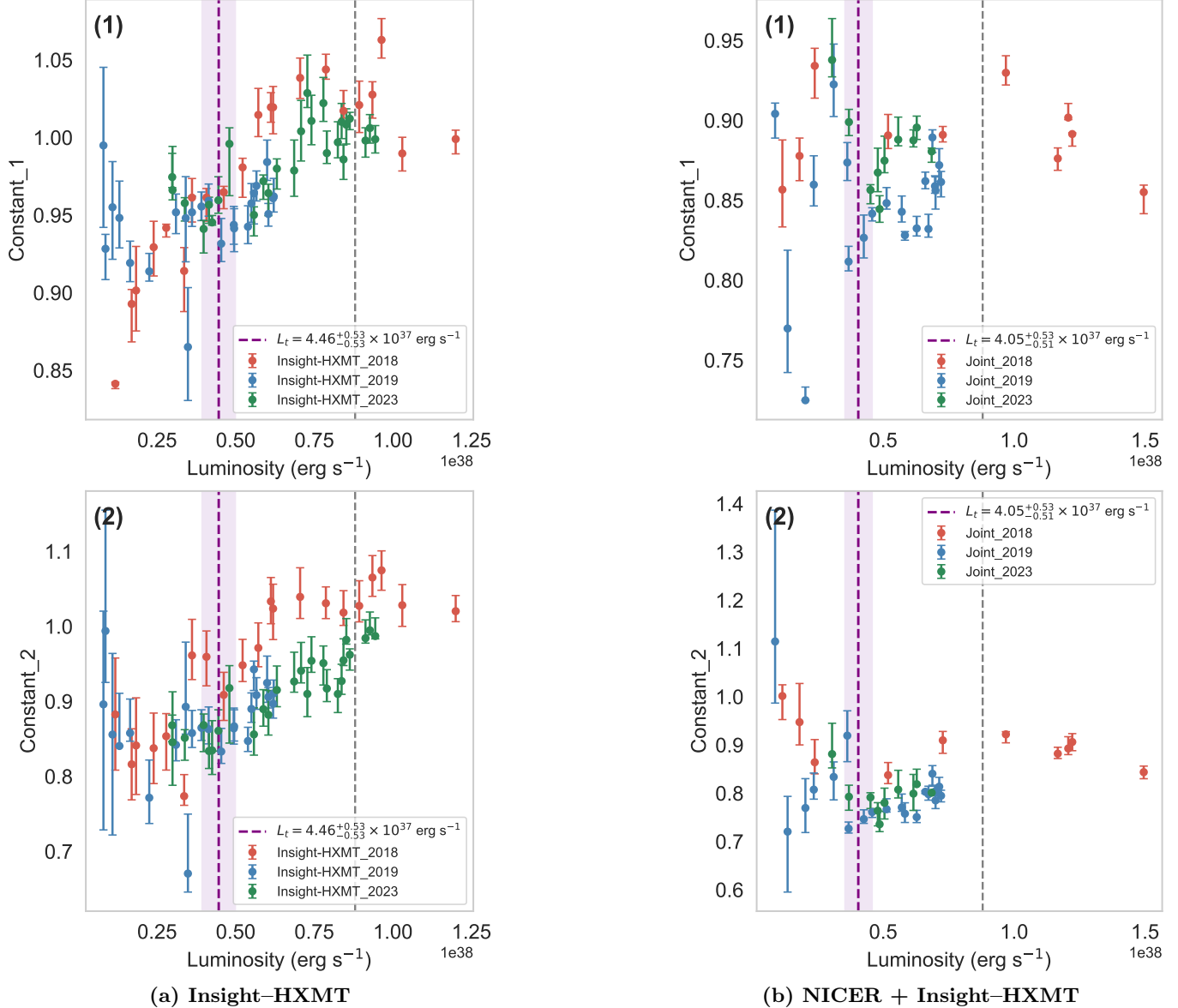


Figure 10. Supplementary to panels (a) and (b) of Figure 2, showing the luminosity dependence of the calibration constants for Insight-HXMT-only and joint fits.

B. MULTIPOLAR SURFACE FIELD FROM EULER POTENTIALS

In an axisymmetric magnetostatic configuration, the magnetic field can be expressed in terms of Euler potentials as

$$\mathbf{B} = \nabla\alpha \times \nabla\beta, \quad (\text{B1})$$

where we choose

$$\alpha = \alpha(r, \theta'), \quad \beta = \phi, \quad (\text{B2})$$

and θ' is the colatitude measured from the magnetic axis (Glampedakis & Lasky 2016; Gralla et al. 2017).

For the “quadrupole” configuration, Lockhart et al. (2019, their Eq. 18) write the Euler potential as

$$\alpha(r, \theta') = B_1 R^2 \frac{R_1^>(r)}{R_1^>(R)} \sin^2 \theta' + B_2 R^2 \frac{R_2^>(r)}{R_2^>(R)} \cos \theta' \sin^2 \theta', \quad (\text{B3})$$

where R is the stellar radius, B_1 and B_2 are the surface dipole and quadrupole coefficients, and $R_\ell^>(r)$ are exterior radial eigenfunctions. On the surface ($r = R$) one has $R_\ell^>(r)/R_\ell^>(R) = 1$, so

$$\alpha(R, \theta') = R^2 [B_1 \sin^2 \theta' + B_2 \cos \theta' \sin^2 \theta']. \quad (\text{B4})$$

Using the definition of \mathbf{B} in spherical coordinates with $\beta = \phi$, one finds that for any axisymmetric $\alpha(r, \theta')$ the radial component of the magnetic field is

$$B_r(r, \theta') = \frac{1}{r^2 \sin \theta'} \frac{\partial \alpha}{\partial \theta'}. \quad (\text{B5})$$

Differentiating Eq. (B4) with respect to θ' and substituting into Eq. (B5) at $r = R$ gives

$$B_r(R, \theta') = 2B_1 \cos \theta' + B_2(3 \cos^2 \theta' - 1). \quad (\text{B6})$$

Evaluating Eq. (B6) at the two magnetic poles yields

$$B_r^N \equiv B_r(R, 0) = 2(B_1 + B_2), \quad B_r^S \equiv B_r(R, \pi) = 2(B_2 - B_1), \quad (\text{B7})$$

where B_r^N and B_r^S are the radial fields at the northern and southern poles, respectively. For prescribed polar field strengths $B_r^N = B_N$ and $B_r^S = B_S$, these relations invert to

$$B_1 = \frac{B_N - B_S}{4}, \quad B_2 = \frac{B_N + B_S}{4}. \quad (\text{B8})$$

Note that B_1 and B_2 are expansion coefficients in the Euler potential rather than the surface polar fields of pure dipole or quadrupole components; for a pure dipole (quadrupole), the corresponding surface polar field is $2B_1$ ($2B_2$).

As an illustrative example, consider a neutron star with surface polar fields

$$B_S = 2.8 \times 10^{12} \text{ G}, \quad B_N = 1.6 \times 10^{13} \text{ G}, \quad (\text{B9})$$

for which Eq. (B8) gives

$$B_{\text{dipole}} = 6.6 \times 10^{12} \text{ G} (2B_1), \quad B_{\text{quadrupole}} = 9.4 \times 10^{12} \text{ G} (2B_2), \quad (\text{B10})$$

so that the quadrupole-to-dipole ratio is $q \equiv B_2/B_1 \approx 1.42$, i.e. the quadrupole and dipole components are of comparable strength while producing highly asymmetric surface polar fields. Even after taking into account the uncertainties of L_t ($4.46_{-0.53}^{+0.53} \times 10^{37} \text{ erg s}^{-1}$) and the CRSF energy ($146_{-4}^{+3} \text{ keV}$) (Kong et al. 2022), we obtain a dipole field strength of $B_{\text{dip}} = 6.6_{-0.2}^{+0.3} \times 10^{12} \text{ G}$ and a quadrupole field strength of $B_{\text{quad}} = 9.4_{-0.3}^{+0.2} \times 10^{12} \text{ G}$, corresponding to a field ratio of $q = 1.42_{-0.06}^{+0.06}$. Notably, the ratio remains larger than unity even when the uncertainties are fully considered (Lockhart et al. 2019).

In vacuum, the exterior multipoles scale as

$$B_1(r) = B_1 \left(\frac{R}{r} \right)^3, \quad B_2(r) = B_2 \left(\frac{R}{r} \right)^4, \quad (\text{B11})$$

so that along the magnetic axis

$$B_r^N(r) = 2[B_1(r) + B_2(r)], \quad B_r^S(r) = 2[B_2(r) - B_1(r)]. \quad (\text{B12})$$

For a canonical neutron-star radius $R_{\text{NS}} = 10 \text{ km}$, an altitude of 300 km corresponds to $r \simeq 31 R_{\text{NS}}$, at which we obtain

$$B_r^N(r) \simeq 2.3 \times 10^8 \text{ G}, \quad B_r^S(r) \simeq -2.1 \times 10^8 \text{ G}, \quad (\text{B13})$$

so that the magnitudes of the northern and southern polar fields differ by only $\sim 10\%$. Defining an effective polar field at this radius by

$$B_{\text{eff}}(r) \equiv \frac{|B_r^N(r)| + |B_r^S(r)|}{2} \simeq 2.2 \times 10^8 \text{ G}, \quad (\text{B14})$$

the surface polar field of an equivalent pure dipole, $B_{\text{p,dip}}$, is determined from

$$B_{\text{eff}}(r) = B_{\text{p,dip}} \left(\frac{R}{r} \right)^3, \quad (\text{B15})$$

yielding

$$B_{\text{p,dip}} \simeq B_{\text{eff}}(r) \left(\frac{r}{R} \right)^3 \simeq 6.6 \times 10^{12} \text{ G}, \quad (\text{B16})$$

which is the surface polar field of a pure dipole that is equivalent, at this radius, to the multipolar configuration discussed above. Thus, at an altitude of 300 km, the quadrudipole configuration is effectively indistinguishable from a pure dipole with $B_{\text{p,dip}} \approx 6.6 \times 10^{12} \text{ G}$.

REFERENCES

Arnaud, K. A. 1996, in Astronomical Society of the Pacific Conference Series, Vol. 101, Astronomical Data Analysis Software and Systems V, ed. G. H. Jacoby & J. Barnes, 17

Bahramian, A., Kennea, J. A., & Shaw, A. W. 2017, The Astronomer's Telegram, 10866, 1

Bailer-Jones, C. A. L., Rybizki, J., Fouesneau, M., Demleitner, M., & Andrae, R. 2021, AJ, 161, 147, doi: [10.3847/1538-3881/ab806](https://doi.org/10.3847/1538-3881/ab806)

Bailer-Jones, C. A. L., Rybizki, J., Fouesneau, M., Mantelet, G., & Andrae, R. 2018, AJ, 156, 58, doi: [10.3847/1538-3881/aacb21](https://doi.org/10.3847/1538-3881/aacb21)

Basko, M. M., & Sunyaev, R. A. 1975, A&A, 42, 311

Becker, P. A., & Wolff, M. T. 2007, ApJ, 654, 435, doi: [10.1086/509108](https://doi.org/10.1086/509108)

—. 2022, ApJ, 939, 67, doi: [10.3847/1538-4357/ac8d95](https://doi.org/10.3847/1538-4357/ac8d95)

Becker, P. A., Klochkov, D., Schönherr, G., et al. 2012, A&A, 544, A123, doi: [10.1051/0004-6361/201219065](https://doi.org/10.1051/0004-6361/201219065)

Burnard, D. J., Arons, J., & Klein, R. I. 1991, ApJ, 367, 575, doi: [10.1086/169653](https://doi.org/10.1086/169653)

Bykov, S. D., Gilfanov, M. R., Tsygankov, S. S., & Filippova, E. V. 2022, MNRAS, 516, 1601, doi: [10.1093/mnras/stac2239](https://doi.org/10.1093/mnras/stac2239)

Cao, X., Jiang, W., Meng, B., et al. 2020, Science China Physics, Mechanics, and Astronomy, 63, 249504, doi: [10.1007/s11433-019-1506-1](https://doi.org/10.1007/s11433-019-1506-1)

Cenko, S. B., Barthelmy, S. D., D'Avanzo, P., et al. 2017, GRB Coordinates Network, 21960, 1

Chen, Y., Cui, W., Li, W., et al. 2020, Science China Physics, Mechanics, and Astronomy, 63, 249505, doi: [10.1007/s11433-019-1469-5](https://doi.org/10.1007/s11433-019-1469-5)

Chhotaray, B., Jaisawal, G. K., Nandi, P., et al. 2024, ApJ, 963, 132, doi: [10.3847/1538-4357/ad235d](https://doi.org/10.3847/1538-4357/ad235d)

Doroshenko, V., Tsygankov, S., & Santangelo, A. 2018, A&A, 613, A19, doi: [10.1051/0004-6361/201732208](https://doi.org/10.1051/0004-6361/201732208)

Doroshenko, V., Zhang, S. N., Santangelo, A., et al. 2020, MNRAS, 491, 1857, doi: [10.1093/mnras/stz2879](https://doi.org/10.1093/mnras/stz2879)

Gendreau, K. C., Arzoumanian, Z., Adkins, P. W., et al. 2016, in Society of Photo-Optical Instrumentation Engineers (SPIE) Conference Series, Vol. 9905, Space Telescopes and Instrumentation 2016: Ultraviolet to Gamma Ray, ed. J.-W. A. den Herder, T. Takahashi, & M. Bautz, 99051H, doi: [10.1117/12.2231304](https://doi.org/10.1117/12.2231304)

Glampedakis, K., & Lasky, P. D. 2016, MNRAS, 463, 2542, doi: [10.1093/mnras/stw2115](https://doi.org/10.1093/mnras/stw2115)

Gralla, S. E., Lupsasca, A., & Philippov, A. 2017, ApJ, 851, 137, doi: [10.3847/1538-4357/aa978d](https://doi.org/10.3847/1538-4357/aa978d)

Inoue, A., Ohsuga, K., Takahashi, H. R., & Asahina, Y. 2023, ApJ, 952, 62, doi: [10.3847/1538-4357/acd6ea](https://doi.org/10.3847/1538-4357/acd6ea)

Jaisawal, G. K., Naik, S., & Chenevez, J. 2018, MNRAS, 474, 4432, doi: [10.1093/mnras/stx3082](https://doi.org/10.1093/mnras/stx3082)

Jaisawal, G. K., Wilson-Hodge, C. A., Fabian, A. C., et al. 2019, ApJ, 885, 18, doi: [10.3847/1538-4357/ab4595](https://doi.org/10.3847/1538-4357/ab4595)

Kennea, J. A., Lien, A. Y., Krimm, H. A., Cenko, S. B., & Siegel, M. H. 2017, The Astronomer's Telegram, 10809, 1

Kong, L. D., Zhang, S., Chen, Y. P., et al. 2020, ApJ, 902, 18, doi: [10.3847/1538-4357/abb241](https://doi.org/10.3847/1538-4357/abb241)

Kong, L.-D., Zhang, S., Zhang, S.-N., et al. 2022, ApJL, 933, L3, doi: [10.3847/2041-8213/ac7711](https://doi.org/10.3847/2041-8213/ac7711)

Kouroubatzakis, K., Reig, P., Andrews, J., & Z., A. 2017, The Astronomer's Telegram, 10822, 1

Lamb, F. K., Pethick, C. J., & Pines, D. 1973, ApJ, 184, 271, doi: [10.1086/152325](https://doi.org/10.1086/152325)

Langer, S. H., & Rappaport, S. 1982, ApJ, 257, 733, doi: [10.1086/160028](https://doi.org/10.1086/160028)

Liu, C., Zhang, Y., Li, X., et al. 2020, Science China Physics, Mechanics, and Astronomy, 63, 249503, doi: [10.1007/s11433-019-1486-x](https://doi.org/10.1007/s11433-019-1486-x)

Lockhart, W., Gralla, S. E., Özel, F., & Psaltis, D. 2019, MNRAS, 490, 1774, doi: [10.1093/mnras/stz2524](https://doi.org/10.1093/mnras/stz2524)

Mushtukov, A., & Tsygankov, S. 2022, arXiv e-prints, arXiv:2204.14185, doi: [10.48550/arXiv.2204.14185](https://doi.org/10.48550/arXiv.2204.14185)

Mushtukov, A. A., Suleimanov, V. F., Tsygankov, S. S., & Poutanen, J. 2015a, MNRAS, 447, 1847, doi: [10.1093/mnras/stu2484](https://doi.org/10.1093/mnras/stu2484)

—. 2015b, MNRAS, 454, 2539, doi: [10.1093/mnras/stv2087](https://doi.org/10.1093/mnras/stv2087)

Nishimura, O. 2014, ApJ, 781, 30, doi: [10.1088/0004-637X/781/1/30](https://doi.org/10.1088/0004-637X/781/1/30)

Postnov, K. A., Gornostaev, M. I., Klochkov, D., et al. 2015, MNRAS, 452, 1601, doi: [10.1093/mnras/stv1393](https://doi.org/10.1093/mnras/stv1393)

Poutanen, J., Tsygankov, S. S., Doroshenko, V., et al. 2024, A&A, 691, A123, doi: [10.1051/0004-6361/202450696](https://doi.org/10.1051/0004-6361/202450696)

Prigozhin, G., Gendreau, K., Doty, J. P., et al. 2016, in Society of Photo-Optical Instrumentation Engineers (SPIE) Conference Series, Vol. 9905, Space Telescopes and Instrumentation 2016: Ultraviolet to Gamma Ray, ed. J.-W. A. den Herder, T. Takahashi, & M. Bautz, 99051I, doi: [10.1117/12.2231718](https://doi.org/10.1117/12.2231718)

Reig, P. 2011, Ap&SS, 332, 1, doi: [10.1007/s10509-010-0575-8](https://doi.org/10.1007/s10509-010-0575-8)

Reig, P., Fabregat, J., & Alfonso-Garzón, J. 2020, A&A, 640, A35, doi: [10.1051/0004-6361/202038333](https://doi.org/10.1051/0004-6361/202038333)

Reig, P., & Nespoli, E. 2013, A&A, 551, A1, doi: [10.1051/0004-6361/201219806](https://doi.org/10.1051/0004-6361/201219806)

Schönherr, G., Wilms, J., Kretschmar, P., et al. 2007, A&A, 472, 353, doi: [10.1051/0004-6361:20077218](https://doi.org/10.1051/0004-6361:20077218)

Serim, M. M., Dönmez, Ç. K., Serim, D., et al. 2023, MNRAS, 522, 6115, doi: [10.1093/mnras/stad1407](https://doi.org/10.1093/mnras/stad1407)

Sokolova-Lapa, E., Gornostaev, M., Wilms, J., et al. 2021, A&A, 651, A12, doi: [10.1051/0004-6361/202040228](https://doi.org/10.1051/0004-6361/202040228)

Staubert, R., Trümper, J., Kendziorra, E., et al. 2019, A&A, 622, A61, doi: [10.1051/0004-6361/201834479](https://doi.org/10.1051/0004-6361/201834479)

Tao, L., Feng, H., Zhang, S., et al. 2019, ApJ, 873, 19, doi: [10.3847/1538-4357/ab0211](https://doi.org/10.3847/1538-4357/ab0211)

Tsygankov, S. S., Doroshenko, V., Mushtukov, A. A., Lutovinov, A. A., & Poutanen, J. 2018, MNRAS, 479, L134, doi: [10.1093/mnrasl/sly116](https://doi.org/10.1093/mnrasl/sly116)

van den Eijnden, J., Degenaar, N., Schulz, N. S., et al. 2019, MNRAS, 487, 4355, doi: [10.1093/mnras/stz1548](https://doi.org/10.1093/mnras/stz1548)

Wang, P. J., Kong, L. D., Zhang, S., et al. 2020, MNRAS, 497, 5498, doi: [10.1093/mnras/staa2448](https://doi.org/10.1093/mnras/staa2448)

Wilms, J., Allen, A., & McCray, R. 2000, ApJ, 542, 914, doi: [10.1086/317016](https://doi.org/10.1086/317016)

Wilson-Hodge, C. A., Malacaria, C., Jenke, P. A., et al. 2018, ApJ, 863, 9, doi: [10.3847/1538-4357/aace60](https://doi.org/10.3847/1538-4357/aace60)

Xiao, H., & Ji, L. 2024, ApJ, 963, 42, doi: [10.3847/1538-4357/ad23cd](https://doi.org/10.3847/1538-4357/ad23cd)

Yamanaka, M., Uemura, M., Nakaoka, T., Kawahara, N., & Abe, T. 2017, The Astronomer's Telegram, 10815, 1

Zhang, S., Lu, F. J., Zhang, S. N., & Li, T. P. 2014, in Society of Photo-Optical Instrumentation Engineers (SPIE) Conference Series, Vol. 9144, Space Telescopes and Instrumentation 2014: Ultraviolet to Gamma Ray, ed. T. Takahashi, J.-W. A. den Herder, & M. Bautz, 914421, doi: [10.1117/12.2054144](https://doi.org/10.1117/12.2054144)

Zhang, S.-N., Li, T., Lu, F., et al. 2020, Science China Physics, Mechanics, and Astronomy, 63, 249502, doi: [10.1007/s11433-019-1432-6](https://doi.org/10.1007/s11433-019-1432-6)

Zhang, Y., Ge, M., Song, L., et al. 2019, ApJ, 879, 61, doi: [10.3847/1538-4357/ab22b1](https://doi.org/10.3847/1538-4357/ab22b1)